metals

MDPI

Article

Atmospheric Corrosion Evolution of Carbon Steel AISI 1020 along a Longitude Transect in the Atacama Desert

Luis Cáceres [1,*], Alvaro Soliz [2] and Felipe Galleguillos [3]

[1] Departamento de Ingeniería Química y Procesos de Minerales, Universidad de Antofagasta, Antofagasta 1240000, Chile
[2] Departamento de Ingeniería en Metalurgia, Universidad de Atacama, Copiapó 1530000, Chile
[3] Centro de Desarrollo Energético de Antofagasta, Universidad de Antofagasta, Antofagasta 1271155, Chile
* Correspondence: luis.caceres@uantof.cl

Abstract: Carbon steel AISI 1020 was exposed to environmental conditions along a transect of the Atacama Desert to gather experimental evidence to identify the local atmospheric mechanism that triggers corrosion through a buildup of water layer formation on the metal surface in addition to corrosion evolution. Coupons initially left in selected sites were periodically collected to determine weight loss and surface attributes by scanning electron microscopy and X-ray diffraction. In addition, meteorological conditions were measured in addition to a fog water collector in one site. During the study period, the predominant conditions were the absence of rain, clear skies, and large daily oscillations in temperature and relative humidity. The evidence indicates a water film formation on a metal surface either from a vertical water flux as fog water droplets and/or by the dew water harvesting mechanism. The uptakes of oxygen and chlorides during the corrosion process were highest in the coastal site P0 and gradually decreased with the increasing distance from the coast. This is attributed to both humidity and saline marine fog intrusion from the coast. The oxide layer evolved to form a compact layer with main constituents of lepidocrocite, goethite, and lesser amounts of akageneite. The corrosion depth can be modelled by a simple power function $d = At^B$ with $B < 1$, indicating a deceleration process.

Keywords: atmospheric corrosion; carbon steel; Atacama Desert; fog formation; SEM; DRX; iron oxides

check for updates

Citation: Cáceres, L.; Soliz, A.; Galleguillos, F. Atmospheric Corrosion Evolution of Carbon Steel AISI 1020 along a Longitude Transect in the Atacama Desert. *Metals* **2022**, *12*, 1980. https://doi.org/10.3390/met12111980

Academic Editor: Gilbert Henaff

Received: 2 October 2022
Accepted: 15 November 2022
Published: 19 November 2022

1. Introduction

Atmospheric corrosion is a degradation of materials explained in terms of an electrochemical process occurring in corrosion cells consisting of base metal, metallic corrosion products, surface electrolytes, and the atmosphere. A list of variables such as relative humidity (*RH*), temperature (T), sulfur dioxide (SO_2) content, hydrogen sulfide (H_2S) content, chloride (Cl) content, amounts of rainfall, dust, and even the position of the exposed metal exhibits marked influence on corrosion behavior of steel exposed to atmospheric conditions. Because this is an electrochemical process, an electrolyte must be present on the surface of the metal for corrosion to occur. In the absence of water/moisture, which is a common electrolyte associated with atmospheric corrosion, metals corrode at a negligible rate. For example, carbon steel parts left in the desert remain bright and tarnish-free over long periods [1].

In carbon steels, iron oxides formed on the surface is loose, porous, and non-protective [2]. Despite this inconvenience, carbon steel is the most widely used steel material in engineering applications. This is because of its significant lower cost in comparison to those of more noble higher-grade alloys, good mechanical properties, and its amenability to be safely operated in very corrosive service conditions under a meticulously designed and implemented control system.

There have been attempts to predict the performance of steel structures over prolonged periods of time as affected by ambient conditions in terms of the corrosion rate and dynamic properties. In a recent review [3], the existing corrosion models were categorized in reference to ISO standards that consider low (C2 level), medium (C3 level), and high (C4 level) corrosivity class levels. In other reviews, a list of parametric models was proposed in terms of parameters that depend on local conditions [4,5].

Atmospheric corrosion-monitoring sensors were employed to study the initial atmospheric corrosion of carbon steels. The results showed that rainfall was the strongest environmental factor influencing the initial atmospheric corrosion rate [6]. The different corrosion sensors that are suitable for corrosion evaluation in atmospheric conditions have been previously published [7].

In the 1980s, three different cooperative studies involving the participation of a large number of countries were carried out, with the first one having the aim of standardizing ISO atmospheric corrosion tests, the second one to obtain the greater knowledge of atmospheric corrosion mechanisms, choosing mathematical models for the calculation of atmospheric corrosion as a function of climate and pollution parameters and elaborating atmospheric corrosivity maps of the Ibero-American region, and finally the third one to perform a quantitative evaluation of the effect of main airborne pollutants as well as climatic parameters on the atmospheric corrosion of important materials. From these studies, a simple correlation for the annual corrosion rate C was developed [8]:

$$C = a_1 + a_2 \cdot RH + a_3 \cdot P + a_4 \cdot T + a_5 \cdot TOW + a_6 \cdot SO_2 + a_7 \cdot Cl, \tag{1}$$

where a_1 to a_6 are constant parameters; RH is the annual average relative humidity in percent; T is the annual average temperature in °C; P is the annual precipitation in mm, TOW is the time of wetness corresponding to the annual fraction of number of hours/year in which $RH > 80\%$ and $T > 0$ °C; SO_2 and Cl are the sulfur dioxide and chloride precipitation in mg/m^2 per day respectively [8].

Several atmospheric corrosion studies for carbon steel have been developed. A measurement campaign from a four-year MITCAT project [8] in 22 rural and urban atmospheres in the Ibero-American region concluded that steel corrosion rates did not differ significantly between them. The only common feature in all these sites was an increase in the passivation character of the steel corrosion product layers with the increase in exposure time [9]. For three years, carbon steel sheets have been exposed to different atmospheres in test sites distributed along the western islands of the Canarian Archipielago in Spain; corrosion values exceeded the established ones of the ISO 9223 norm [10].

Carbon steel test pieces were exposed to a variety of environmental conditions in Gran Canaria Island. The chloride ions and the time of wetness were the most significant factors in the corrosive process, while SO_2 was of significance only in marine-industrial areas [11]. A significant compaction of the rust layers was found in low polluted-areas during a long-term atmospheric corrosion of mild steel in different rural and urban localities in Spain [12].

In the coastal and inland areas of the Atacama Desert, the availability of water is restricted to dew formation and occasional rains that occur approximately once every 10 years apart [13–16]. Several investigations have found a direct relationship between air pollution and high concentration of pollutants in collected water samples during foggy days [17–19]. Fog water collected from non-polluted air have been found to be an attractive source of water for human consumption as is the case of Northern Chile. Among the large amount of available information concerning atmospheric corrosion of carbon steel, there is little information on Atacama's analog conditions dealing with corrosion mechanism. Given its extreme aridity, the Atacama Desert has been chosen as a model for the planet Mars to develop several studies on life-limiting conditions [20–22].

In this work, we investigated the atmospheric corrosion of carbon steel coupons along a transect of the Atacama Desert to gather experimental evidence to identify the local atmospheric mechanism that triggers corrosion through a buildup of water layer formation on the metal surface. Thus, the novelty of this research lies in its focus of devising the mechanism of water layer formation on a metal surface with subsequent corrosion in the absence of rainfall as is the case of the Atacama Desert. The hypothesis of this research is that in the absence of rainfall, a water layer thickness on the metal surface can be formed by an advective mechanism by which water fog droplets grow at mid altitudes and further precipitates and/or by a radiative mechanism overnight as the air near the ground cools and stabilizes. For this purpose, carbon steel coupons were deposited in selected sites of the Atacama Desert with temperature and relative humidity sensors and removed at predetermined times for data retrieval and morphological inspection of the coupons. The interpretation of the observed oxide features is linked with moisture indicators of ambient conditions.

2. Materials and Methods

2.1. Material Preparation

Five experimental sites were selected within 80 km along the local road to the Chilean Escondida Mining complex from the coast of Antofagasta up to 900 m above sea level situated in a west–east (W–E) direction, which are described in Table 1.

Table 1. Geographical locations of the selected experimental sites.

Site	Coordinates		Coupons and Devices
	Position (WGS84)	Altitude (m)	
P0	23°43.020′ S 70′25.187′ W	20	11 coupons on the ground and one T/RH sensor One meteorological station with 9 sensors: University of Antofagasta (UA)
P1	23°45.563′ S 70′15.769′ W	570	11 coupons on the ground and T/RH sensor
P2, P2A	23°44.773′ S 70′11.106′ W	655	P2: 11 coupons on the ground and one T/RH sensor P2A: one T/RH sensor above 3 m over the ground
P3, P3A	23°51.964′ S 69′50.956′ W	789	P3: 11 coupons on the ground and one T/RH sensor P3A: one fog water collector and one T/RH sensor above 3 m over the ground
P4	23°56.606′ S 69′43.781′ W	915	11 coupons on the ground and one T/RH sensor

In all experimental sites (Figure 1), 16 identical squared coupons with dimensions of $12 \times 12 \times 2$ mm^3 and one temperature and relative humidity sensor were placed on the bare ground together with complementary devices described as follows: In the P0 site at the campus of the Antofagasta University, there was a meteorological station HOBO Model RX3000 Station (ONSET Corp., Bourne, MA, USA) with temperature, relative humidity, velocity, and direction of wind, pressure and solar radiation sensors on a lab roof which was 5 m over the ground. In the P2 and P3 sites, one additional temperature−relative humidity sensor was attached to a pole at 2 m above the ground surface. In addition, in the P3 site, an apparatus to collect water from fog according to a design described in a former work [23] was installed (Figure 2). This fog collector consisted of a 35% shade polypropylene Raschel mesh secured by a 1×1 m^2 rigid metal frame held in place by equally spaced high-strength wires as lateral supports. The frame orientation was along the E−W axis, the prevailing direction of the wind. Below the frame, an inclined trough allowed water to flow toward an automatic rain gauge. The collected fog water was automatically recorded in a logger from a tipping recorded bucket type rain gauge (Hobo Onset logging rain gauge model RG2-M—ONSET Corp., Bourne, MA, USA). Time and date stamps were stored in the logger for each 0.2 mm tip event for detailed analysis. A T/RH Hobo sensor was placed at the side of the fog water collector.

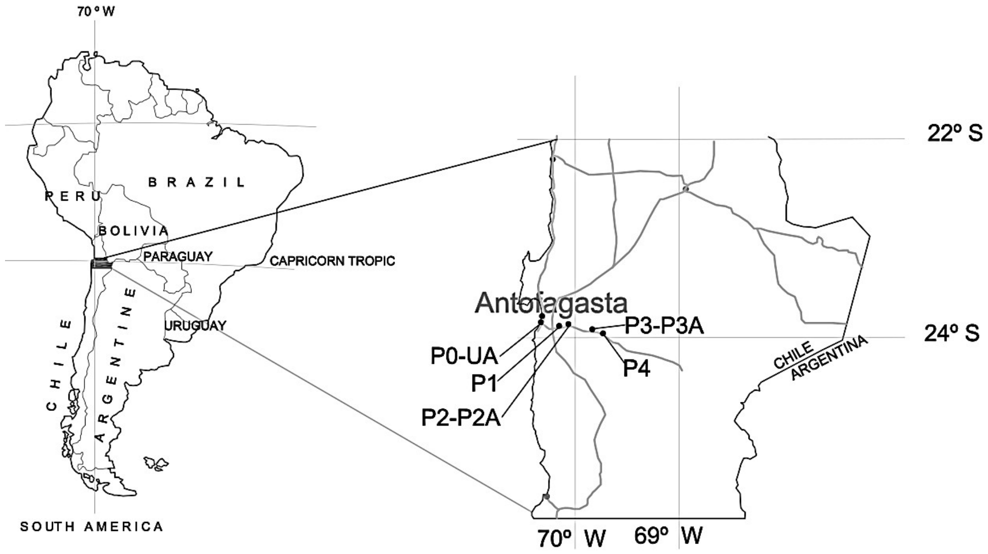

Figure 1. Map of experimental sites.

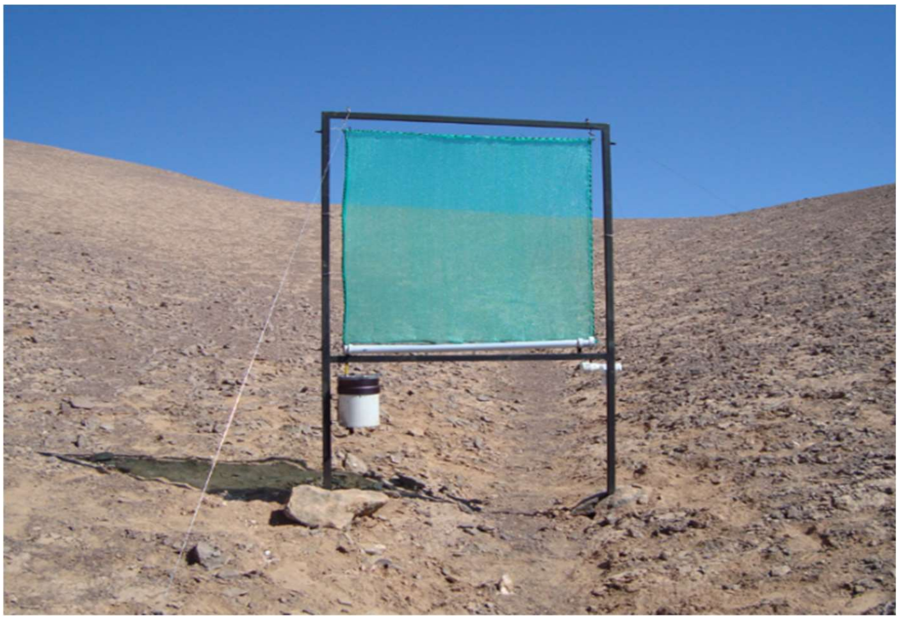

Figure 2. Fog water collector positioned nearby the P3 site. A 1 × 1 m^2 polypropylene Raschel mesh was mounted in a metal frame structure. It was equipped with a T/RH Hobo logger sensor (bottom right side) and a Hobo Onset logging rain gauge model RG2-M (bottom left side).

2.2. Corrosion Density Rate Measurements

The test material was carbon steel AISI 1020 coupons with chemical composition (in wt %) of 98.5% Fe, 0.2% C, and 0.6% Mn and traces of P, S, Si, Sn, Cu, Ni, Cr, and Mo. At each site, four coupons at three different dates during 234 days of exposure were collected for corrosion rate measurements and morphological characterization. Corrosion rates by loss of weight were measured according to standard procedures [24].

2.3. Morphological and Patterns Characterization

A Zeiss EVO MA 10 scanning electron microscope (SEM) (Zeiss, Oberkochen, Germany) equipped with an energy-dispersive X-ray (EDS) analyzer was used for morphological characterizations. A Shimadzu XRD-600 diffractometer (Shimadzu Corp., Kyoto, Japan) using Cu Kα radiation at an angular step of 0.02° (2θ) and a counting time per step of 4 s was used for the determination of the main corrosion products.

3. Results and Discussion

3.1. Meteorological Characterization and Daily Cyclic Precipitation of Water

Meteorological data in all experimental sites were measured from 24 October 2021 to 18 June 2022 (Table 1). In general, temperature and relative humidity values (Figure 3) had a daily cyclic variation with the maximum and minimum relative humidity daily values taking place at early morning and afternoon hours, respectively, as opposed to temperature values. The daily cyclic amplitudes for both *T* and *RH* were heavily dependent upon their distances to the coast with a trend starting from the lowest amplitude values at the coastal P0 site and gradually increasing toward inland sites (Table 2). This amplitude trend is due to a combination of the quasi-permanent influence of the southeast Pacific subtropical anticyclone in Northern Chile that forces year-round equatorward cold winds along the coast flowing inland from the Pacific [25,26] and high solar irradiance [27,28]. The wind speed and its direction exhibited a daily pattern of a distinctive wind direction emanating from the SE direction during afternoon hours; over this period, the maximum wind velocities (between 2 and 6 m/s) took place (Figure 4); during the rest of the day, wind velocities were lower than 2 m/s with a randomly changing direction between W and N. This wind pattern associated to predominant periods of radiative air heat and cooling [29] was coincident with 1997 wind data reported at Yungay, an inland location 50 km south of the P4 site [16].

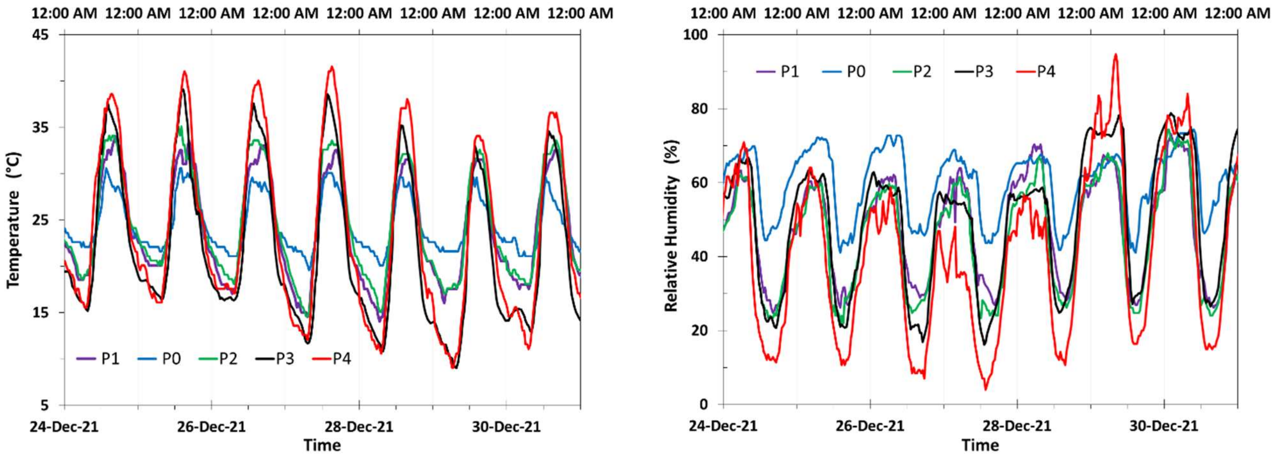

(**a**) (**b**)

Figure 3. One-week temperature (**a**) and relative humidity (**b**) measurements from ground-level sensors.

Table 2. Global average and average oscillations of temperature and relative humidity values from 24 October 2021 to 18 June 2022.

Site	Average Values		Average Daily Oscillations	
	Temperature °C	Relative Humidity %	Site	Temperature °C
P0	20.6	58.0	P0	20.6
UA	18.1	73.9	UA	18.1
P1	17.3	54.9	P1	17.3
P2	18.1	49.8	P2	18.1
P2A	18.4	63.7	P2A	18.4
P3	18.8	40.2	P3	18.8
P3A	17.0	59.2	P3A	17.0
P4	19.6	27.6	P4	19.6

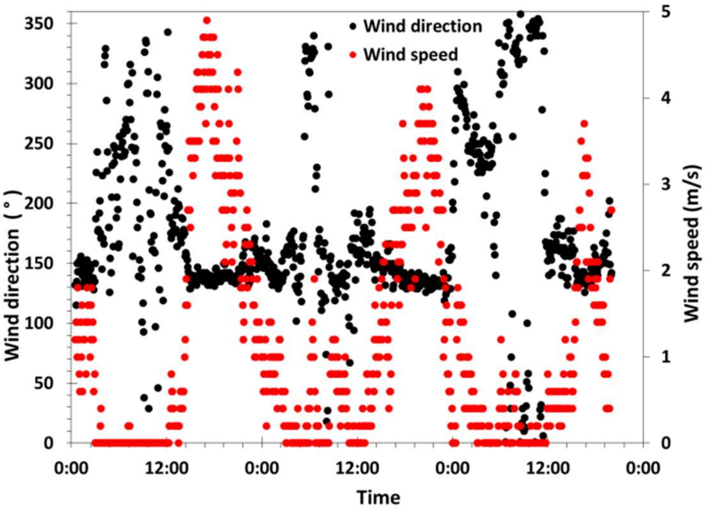

Figure 4. Wind directions and speeds at the coastal station (P0) measured between 22 January 2022 and 24 January 2022.

Figure 5 shows the daily average temperature and relative humidity values during all measurement campaigns. Two main interesting features observed from these data were the seasonal temperature trend by which the minimum and maximum values occurred in winter (May to September) and summer (December to April), respectively, and the apparent vertical temperature profile that emerged from measurements from ground and aboveground positioned sensors. For instance, aboveground sensors at P2A and P3A sites indicate significant lower temperature values than ground sensors; this difference was notoriously higher in warmer seasons. In contrast, the *RH* aboveground values were significantly higher than those at ground *RH* values. Specifically, while homogeneous *RH* values up to 90% occurred above the ground, ground-level *RH* values followed a seasonal trend with values up to 60% and 40% *RH* in warmer and colder seasons, respectively.

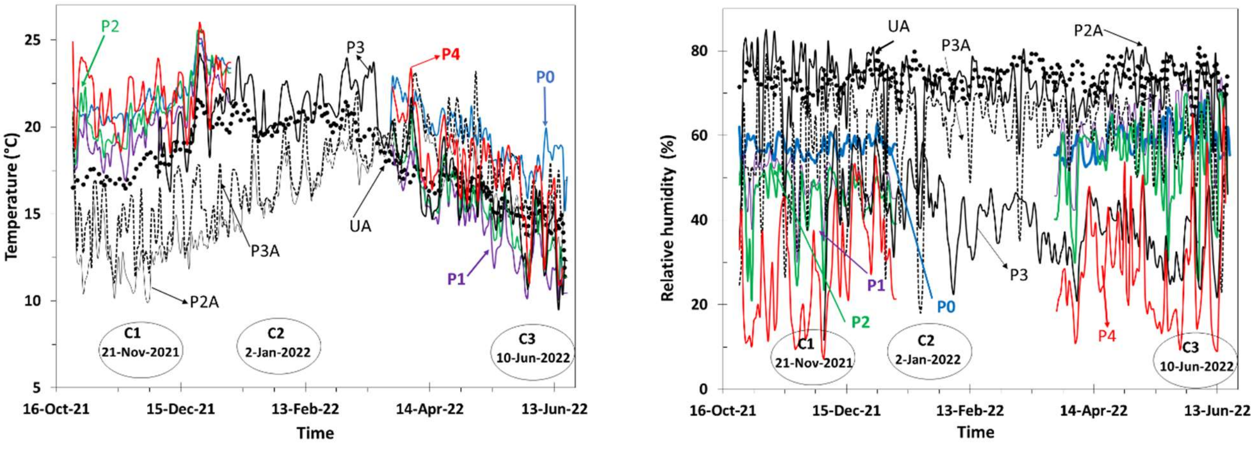

(**a**) (**b**)

Figure 5. Daily average temperature (**a**) and relative humidity (**b**) values from 24 October 2021 to 18 June 2022, measurements by ground-level sensors.

Figure 6 shows the typical daily patterns for the *T* and *RH* vertical gradients in three different sites. In the coastal site, the daily temperature cycle started at night hours as a constant positive value until early morning, then increased up to the maximum at midday and finally decreased to the minimum negative value at late afternoon. Vertical gradient patterns observed in P2 and P3 sites, which resembled each other, differed from that of P0 pattern in several aspects. First, the maximum peaks for P2 and P3 had significant larger values. Second, the maximum peaks for P2 and P3 were delayed in at least 3 h in comparison to the P0 maximum peaks. Third, instead of the constant peak values observed for P2 and P3, a decreasing trend up to the minimum negative value during the morning was identified for P0.

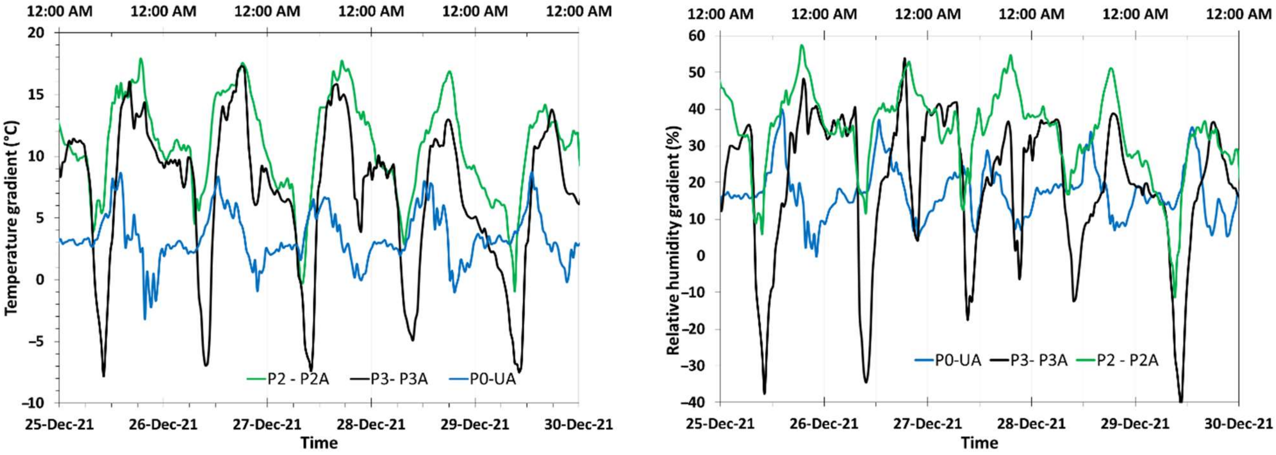

(**a**) (**b**)

Figure 6. Temperature (**a**) and relative humidity (**b**) vertical gradients in 3 different sites expressed as differences between measured values from sensors positioned at the ground and 5 m above the ground, respectively (refer to Table 1).

Fog formation, a process that is associated to high relative humidity values, occurs preferentially at certain topographical formations in the Atacama Desert where air cooling occurs [14,15,30]. Figure 7 shows periods of fog precipitation that occurred in the fog collector (Figure 2) at site P3A, whose design efficiency have been proven in earlier investigations [23,31]. Fog water collection above the ground is an evidence of soil wetting in terms of falling water droplets formed above the ground, where *RH* values were much higher than those at the ground level. This *RH* vertical profile that converged from high values above the ground to low values at the ground level could be originated from differing cooling rates between air mass and soil surface. Figure 5 indicates a significantly larger relative humidity values at UA, P2A, and P3A with respect to the corresponding ground values (P0, P2, and P3) between March and the end of July 2022, a period when frequent fog collection was recorded.

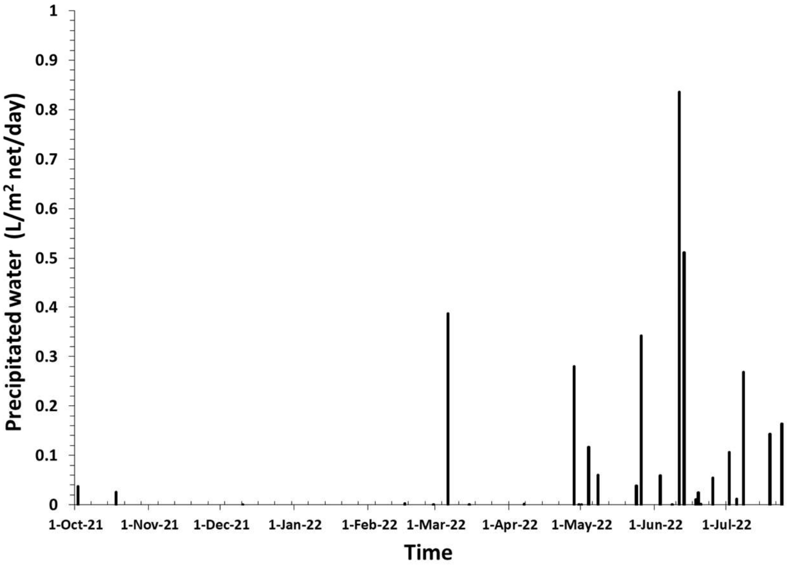

Figure 7. Precipitated fog water events in a fog water collector at site P3 (refer to Table 1).

3.2. Time of Wetness (TOW)

A definition of *TOW* is the time during which the *RH* of the ambient environment is greater than a threshold *RH* value at temperatures above 0 °C. This definition is based on the idea that above a certain humidity threshold, corrosion increases substantially due to sorption of water on the surface. The basis for a critical humidity value is unclear, and this threshold has been shown to be a highly inaccurate estimate for actual surface wetness in certain outdoor environments [32]. The chosen limiting relative humidity value for this calculation depends on the metal and many local conditions; for iron, the critical value is in the range of 60–80% [33,34].

For the present investigation, the time of wetness in the absence of rainfall was determined as the time in hours per month, during which the relative humidity values were equal or higher than 80% and the temperature were higher than 0 °C [35]. An important local condition is an exceptionally low content of contaminants in fogs [36]. Experimental *TOW* values measured in all sites as h/month are shown in Figure 8. Three important features of these values were as follows: first, all *TOW* values that ranged between 0 and 20 h/month (equivalent to 0 to 240 h/year) fell within categories 1 and 2 [35]; the most severe case of category 5 corresponded to values exceeding 5500 h/year. Second, the *TOW* values in all sites took place in shorts periods at nighttime approximately between 12 p.m. and 8 a.m. Third, the inland Atacama Desert is exceptionally free of clouds with high solar radiation; this condition is prevalent over the years [16,23,37].

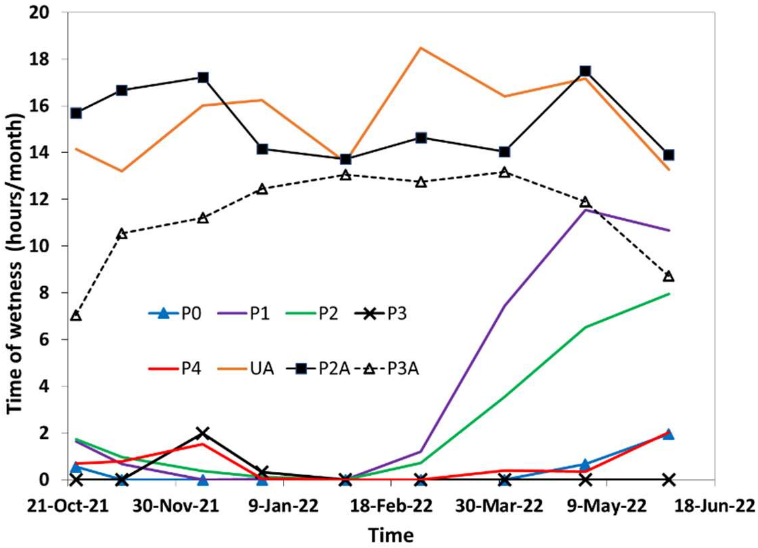

Figure 8. Time of wetness values determined from the measured relative humidity values at all sensors.

It was observed that a metal surface wetting took place at early hours every day, only if *RH* is greater than 80%, in other words during *TOW* periods. Once a water film was formed during early morning, an evaporation process began because of the increasing solar intensity that was combined with a decreasing trend of *RH* values in the air (Figure 3). In comparison to the water evaporation rate in open ponds (whose values in Atacama Desert ranges between 7 to 12 mm/day [35]), the water film deposited on a bare metal surface directly exposed to a sunshine evaporated faster because of a rapid temperature increase of sun-heated surfaces together with a decrease of *RH* values. Thus, the water film formation on the metal surface exposed to Atacama's ambient condition took place as a sequential dry/wet daily cycling with a maximum average wet period of 40 min.

The absolute humidity (*AH*) expressed as kg water/kg dry air is a measure of the actual amount of water vapor (moisture) in the air, regardless of the air's temperature; this value was computed using the following standard correlation [38]:

$$AH = \frac{M_w \cdot P_w}{M_A \cdot (P_{atm} - P_w)}, \tag{2}$$

where M_w is the molecular weight of water with a value of 18.02 g/mol, M_A is the molecular weight of air equivalent to 28.97 g/mol, P_{atm} is the atmospheric pressure equal to 760 mm Hg, and P_w is the partial pressure of water in mm Hg.

P_w was computed from *RH* and P_s values as:

$$P_w = \frac{RH}{100} \cdot P_s, \tag{3}$$

where P_s is the saturated pressure of water at a defined temperature *T* and a pressure of 1 atm.

P_w was computed as:

$$AH = \frac{0.622 \cdot RH \cdot P_s}{(760 - 0.8 \cdot P_s)}. \tag{4}$$

Considering a fitted P_s expression valid for a *T* range between 5 and 30 °C, the value in mmHg can be determined by:

$$P_s = 0.026 \cdot T^2 + 0.0833 \cdot T + 5.6768, \tag{5}$$

where *T* is in °C.

From those expressions, *AH* values of 0.0084, 0.0097, and 0.0134 g water/g dry air for 15, 17, and 21 °C, respectively, were computed at an *RH* value of 80%. These values demonstrate a significant temperature influence on the water content of ambient air at a fixed *RH* where *TOW* is computed.

3.3. Corrosion Distribution and Patterns

A necessary condition for corrosion of carbon steel coupons in the absence of rain is a water film formation on the metal surface. As discussed in the preceded section, this took place as daily sequential wet/dry periods only in those occasions when the maximum daily *RH* values exceeded over 80%. It was also shown that the amount of available water (absolute humidity) under a fixed *RH* humidity value was greater at higher temperatures. This circumstance creates a need to also define a temperature as a reference.

Corrosion expressed as mass loss (also called corrosion depth) per area measured at 32, 74, and 241 days of exposure in sites P0 to P4 (Figure 9) indicated that the highest values for coupons collected at times t_1 and t_2 took place at the coastal site P0. In this site, the measured temperature and *RH* values (Figure 5) were highest at ground and aboveground sensors, respectively. In contrast, for time t_3, these values were quite similar in comparison to those measured in the other sites; the highest mass loss shown by P1 was corroborated by the highest *RH* values ever measured of all ground sensors (Figure 5). Although no aboveground *RH* measurements were made at the P1 site, the evidence from sites P0, P2, and P3 suggests high *RH* values for P1. The lowest corrosion values observed in P4 site were again compatible with comparatively high *T* and low *RH* values. The corrosion trend in P2 is inconsistent in that the low corrosion rates were not compatible with temperature and *RH* measurements shown in Figure 5. The lowest temperature values at the P2 site during the first three months of exposure as compared with all other sensors could explain this anomaly. An interesting observation in site P3 is the occasional presence of wind-driven dust over the surface of coupons. In considering the corrosion values such as those of P2 and P4, the effect of dust deposition can be disregarded.

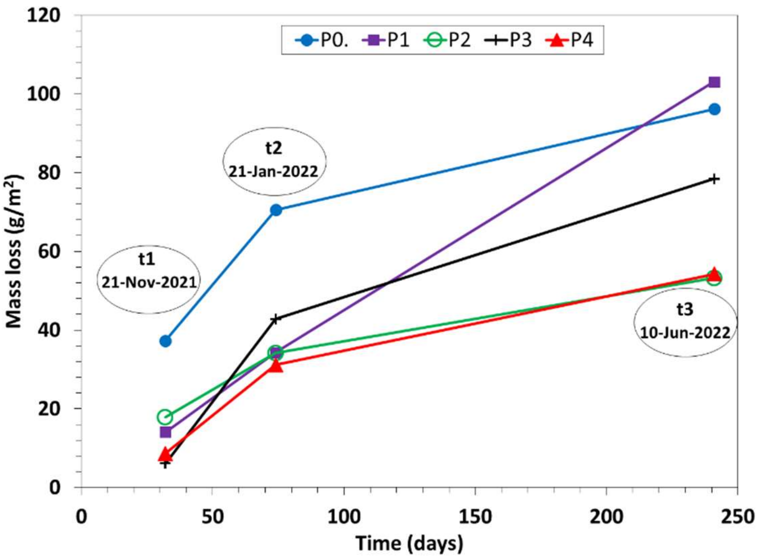

Figure 9. Corrosion rates measured at 32, 74, and 241 days of atmospheric exposure of coupons at the P0, P1, P2, P3, and P4 sites.

The lowest atmospheric corrosion depth for carbon steel ever reported as mass loss indicates values between 8 and 30 g/m^2 during 250 days of exposure [39]; no details were given about ambient conditions. In a previous detailed investigation [40], carbon steel exposed to outdoor wet-dry cyclic ambient conditions categorized as C3 [35] presented the maximum mass loss value of 240 g/m^2 after 200 days which is twice as much the maximum value obtained in the present investigation.

Among the existing numerical models to simulate atmospheric corrosion for a long-term, a simple power function model is shown as follows [3,5]:

$$d = A{\cdot}t^B, \tag{6}$$

where d is the corrosion depth, t is the time of exposure in year, and A and B are constants. If $B > 1$, the corrosion process is accelerated. Alternatively, in the case of $B < 1$, the deceleration of process governs the corrosion loss, and if $B = 1$, the corrosion rate is constant.

It is clear from the shape of the mass loss curves for different sites that $B < 1$ which suggests that under Atacama's ambient conditions, the exposed carbon steel passivates with time. This deceleration shape seen on corrosion rates plots (Figure 9) was validated at a longer time with a single mass loss value of carbon steel coupons in triplicate left at the P0 site on 6 October 2020. This mass value measured at the time of the present investigation was 176 g/m^2 after 710 days of exposure.

The argument that the metal surface wetting mechanism is through a falling water droplet generated at high *RH* values above the ground level clearly invalidates the use ground *RH* values for *TOW* calculation. In fact, Figure 8 indicates too low *TOW* values for all ground sensors, while the *TOW* from aboveground sensors had reasonable values. In addition, the significant effect of temperature on the available water also indicates that *TOW* based on an *RH* threshold is an inadequate index to be used in arid regions. Perhaps a reference temperature, in addition to an *RH* value of 80%, should be defined to determine an absolute humidity value as a threshold. Then, experimental temperature and *RH* values must be used to calculate absolute humidity for a subsequent *TOW* determination.

3.4. Surface Morphology and Elemental Analyses

Surface and elemental analyses of the coupons at different corrosion times (Figures 10–15 and Table 3) illustrated progressive changes in surface morphology and composition. From the overall results, distinctive morphological features were observed. From Figure 10, the initial coupons showed a smooth surface with superficial scratches left from using sandpaper during the abrading process. It can be observed that the coupons exposed to atmospheric corrosion in the Atacama Desert were already oxidized during the first 32 days of exposure with the random formation of corrosion products on the metallic surface (Figures 11a, 12–14 and 15a). It is apparent that the corrosion was initiated in random spots that further evolved to large aggregates that increased at longer exposure times (Figures 11d, 12–14 and 15d). The largest initial mass loss value for 32 h of exposure at the P0 site (Figure 9) was compatible with the largest number of oxides seen at this time (Figure 11a). During this period, the corrosion rate, visualized as the slope of the mass loss curve in Figure 9, had the maximum values. It is interesting to note that the rust layer was dense and attached to the surface so that it acted as a barrier to effectively inhibit the diffusion of oxygen and corrosive electrolytes, leading to a decreasing corrosion rate evolution.

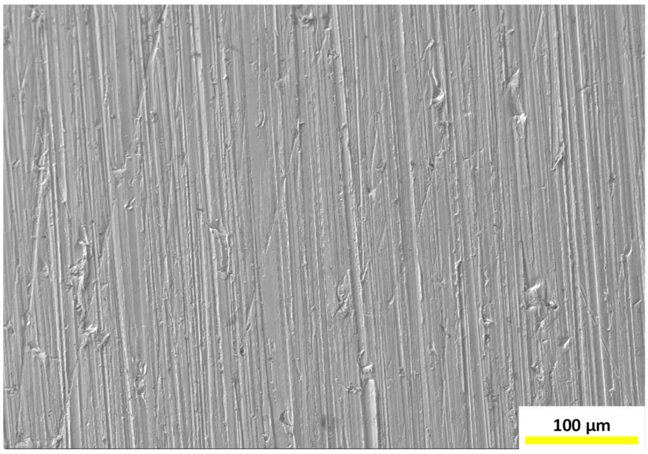

Figure 10. SEM photograph of a polished coupon.

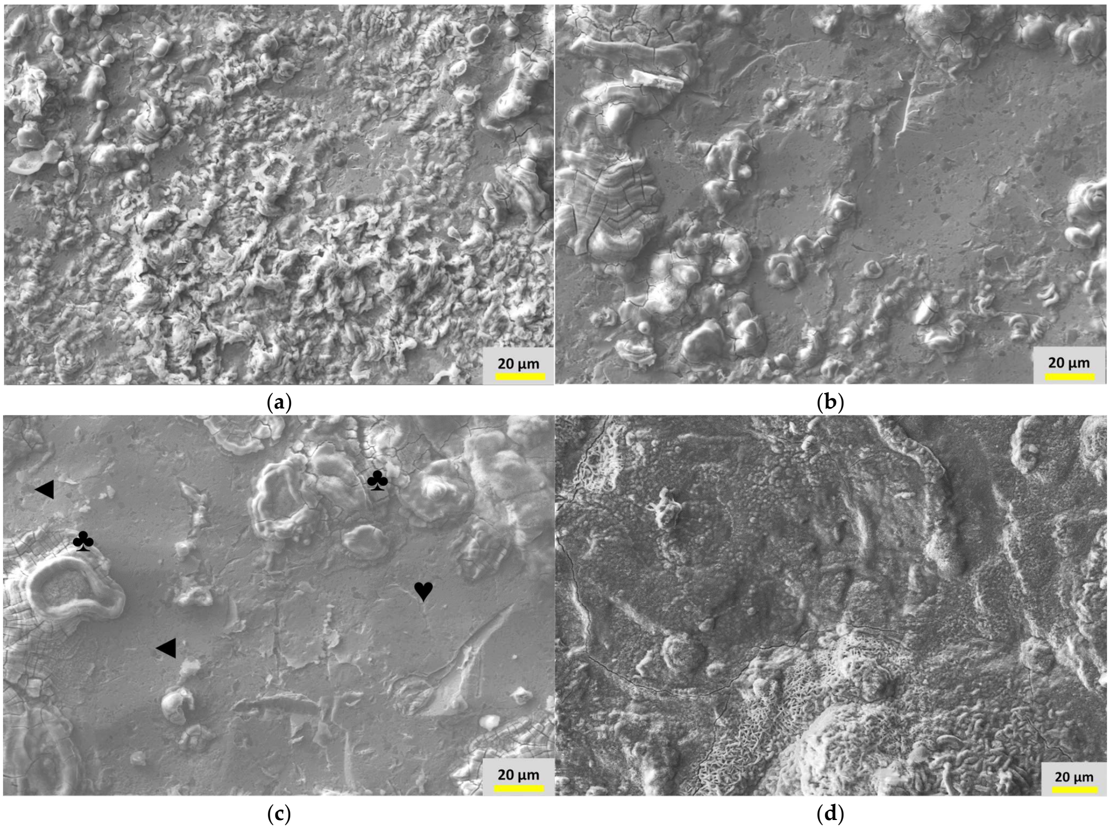

(**a**) (**b**)

(**c**) (**d**)

Figure 11. SEM photographs of carbon steel samples in position P0 at 32 days (**a**), 74 days (**b**), 120 days (**c**), and 241 days (**d**) of exposure.

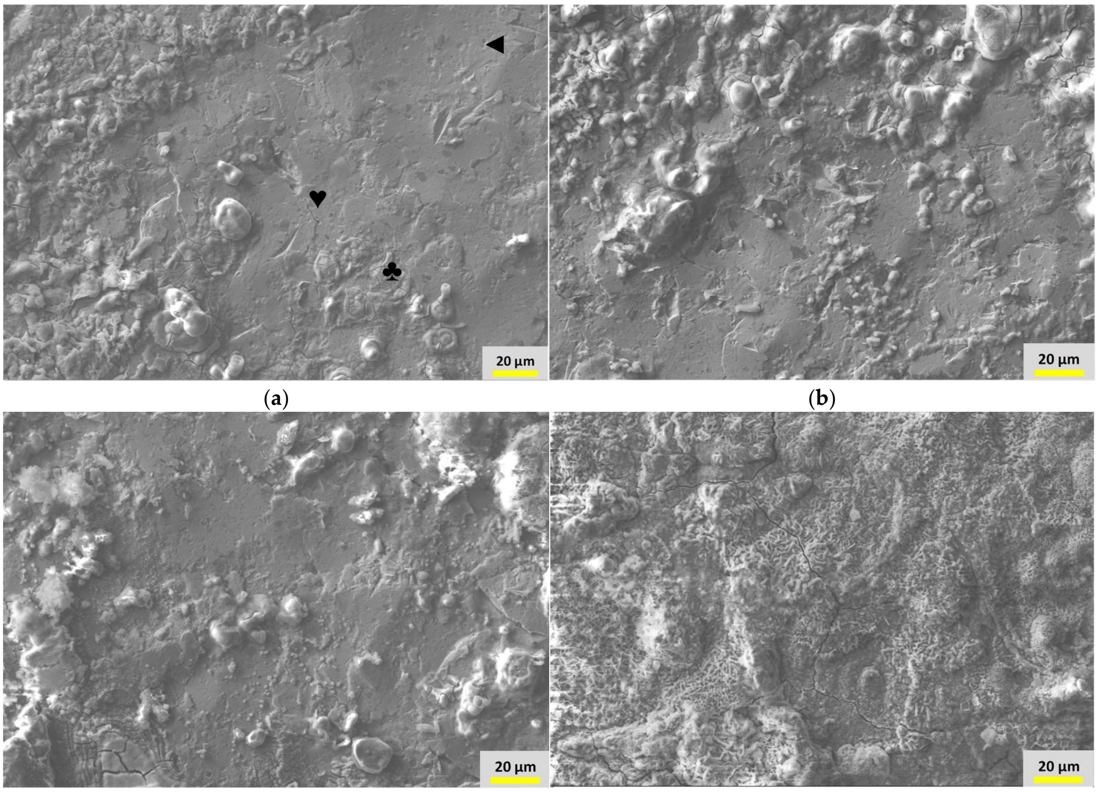

(**a**) (**b**)

(**c**) (**d**)

Figure 12. SEM photographs of carbon steel samples in position P1 at 32 days (**a**), 74 days (**b**), 120 days (**c**), and 241 days (**d**) of exposure.

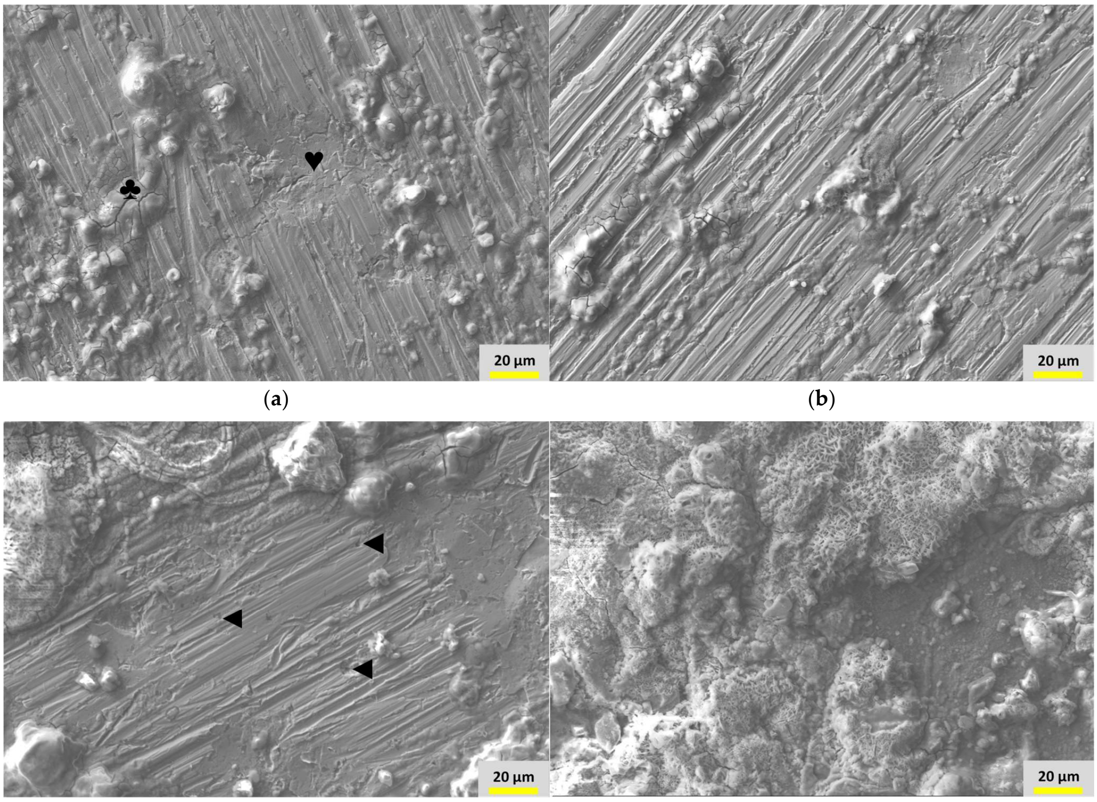

(**a**) (**b**)

(**c**) (**d**)

Figure 13. SEM photographs of carbon steel samples in position P2 at 32 days (**a**), 74 days (**b**), 120 days (**c**), and 241 days (**d**) of exposure.

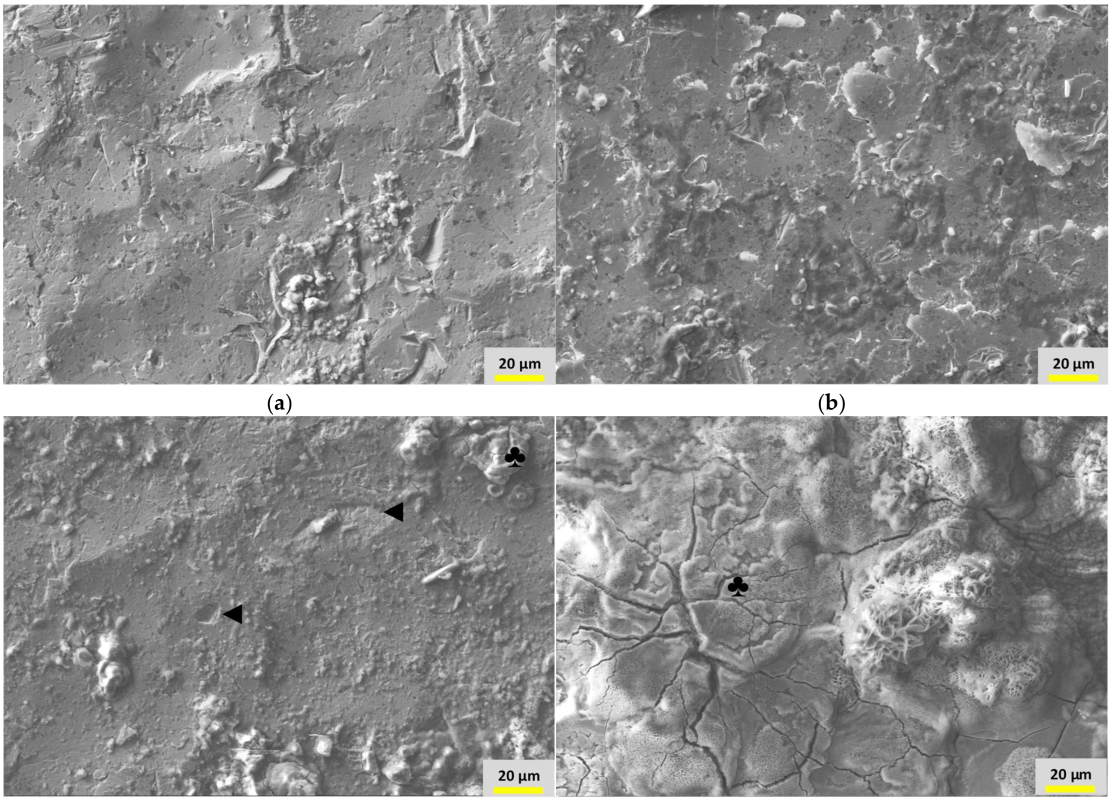

(**a**) (**b**)

(**c**) (**d**)

Figure 14. SEM photographs of carbon steel samples in position P3 at 32 days (**a**), 74 days (**b**), 120 days (**c**), and 241 days (**d**) of exposure.

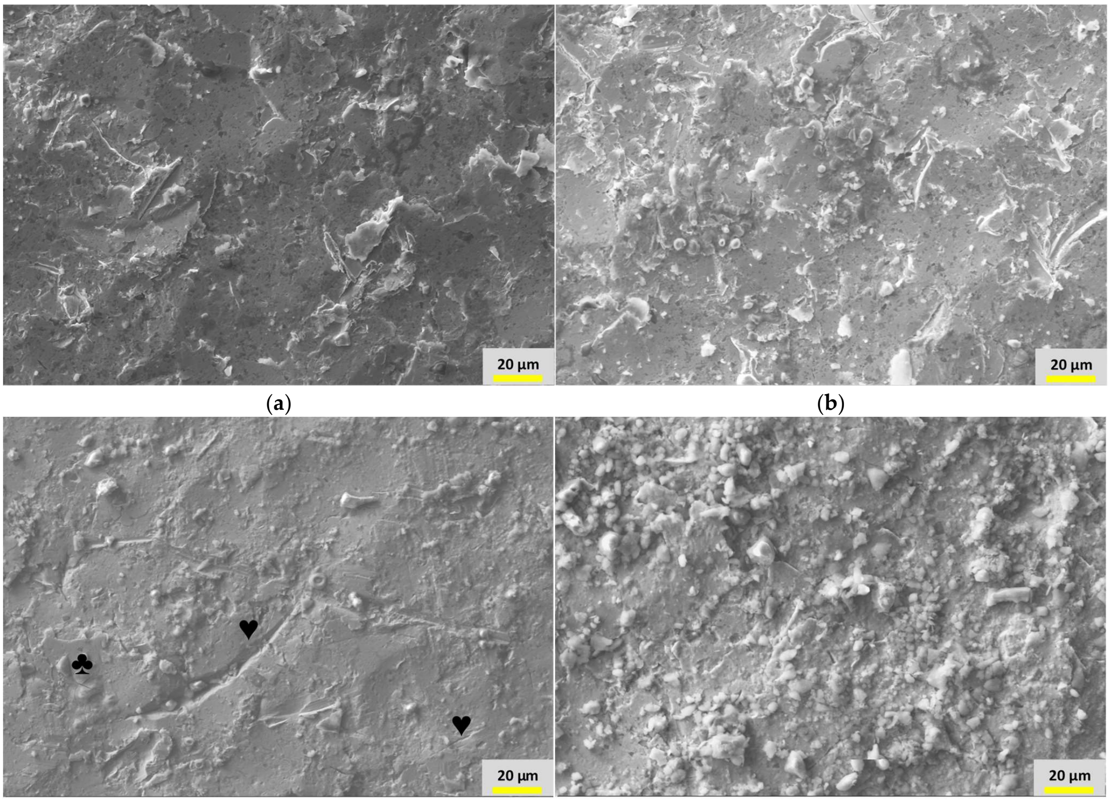

(**a**) (**b**)

(**c**) (**d**)

Figure 15. SEM photographs of carbon steel samples in position P4 at 32 days (**a**), 74 days (**b**), 120 days (**c**), and 241 days (**d**) of exposure.

Table 3. Elemental analyses of the surface coupons after 32-day exposure, measured by EDS analysis.

Element (%)	**AISI 1020 Composition**	**Sites**				
		P0	**P1**	**P2**	**P3**	**P4**
Fe	98.5	67.3	77.6	86.2	86.4	88.3
O	-	24.4	13.8	5.8	5.6	4.3
C	0.2	5.7	5.8	5.5	4.8	4.6
Si	Traces	0.7	1.2	0.6	1.4	1.5
Cl	-	0.5	0.2	0.1	0.1	-
Na	-	0.4	0.3	0.1	0.3	0.2
Mn	0.6	0.3	0.5	0.6	0.5	0.6
Al	-	0.3	0.3	0.3	0.5	0.2
Ca	-	0.1	0.3	0.2	0.2	0.3
S	Traces	0.1	0.1	0.1	0.1	-
Cr	Traces	0.1	-	-	-	0.1
Co	-	-	-	0.4	-	-

All the samples had similar corrosion morphologies, and the damaged areas can be categorized as a general corrosion mechanism containing pits (symbol ◄ in figures) and cracks on the corrosion products layer (symbol ♣ in figures) and the metallic surface (symbols ♥ in figures). Individual pits are not fully visualized, probably because they were superimposed as result of the initial highest corrosion rate (Figure 8). However, pits randomly grew, leaving dispersed uncorroded areas (see ◄ in Figure 13c).

Additionally, cracks formation observed in the metallic surface and the corrosion product layer are a result of the daily wetting−drying cycles. No distinctive morphological features can be attributed to any of the coupons, in other words, the morphological evolution of the oxide layer that is location-independent is in direct relation with its corrosion rate value. It can be observed after many months of exposure time the presence of a dense oxide layer on all coupons, with areas containing flowery structures typical of a lepidocrocite phase (γ-*FeOOH*) (Figures 11d, 12–14 and 15d). This oxide layer pattern has been observed by many investigators [2,12,41].

The elemental composition measured after 32 days of exposure (Table 3) showed a significant oxygen uptake that was more pronounced in the coastal site P0 and decreased in P1 and approximately constant in P2, P3, and P4. The similar trend, but at much lower concentration, shown for sodium and chloride, suggests marine fog intrusion had the maximum intensity in the P0 site and from there experienced a notorious decrease in intensity from P2 to P4. Intriguing is the apparent carbon uptake by oxidized coupons from 0.2% to more than 5%; although no reference has been found concerning atmospheric carbon uptake associated to metal corrosion processes, abiotic CO_2 uptake from the atmosphere in semiarid desert soils is a controversial issue that arose from positive experimental measurements [42]. Probably the source of carbon is deposited dust on a coupon surface that actively uptake CO_2 from the atmosphere. Dust deposited on coupons in this work was evidenced from the positive presence of Si, Ca, and S (Table 3).

3.5. Oxide Evolution

Diffraction peaks due to the oxide layer were observed in Figure 16. Goethite, lepidocrocite, and akageneite were the three main oxides identified in each corrosion coupon. Visual identification of lepidocrocite at longer exposure time indicated gradual evolution from amorphous oxides toward crystalline oxide forms. According to the literature [43,44], in the wet periods, the dissolution of iron is balanced by the cathodic reduction of Fe(III) oxides, usually $\gamma - \text{FeOOH}$, giving rise to magnetite that later in dry periods is re-oxidized by oxygen. After several wet–dry cycles, the reduction of thin dense electrodeposited $\gamma - \text{FeOOH}$ layers to form magnetite do not occur; in addition, the formation of $\alpha - \text{FeOOH}$ in such conditions is also possible. Many other iron oxides species can be formed under specific conditions. For example, under the condition with a low salt deposition rate, the accumulation of salt without wash effects is essential for akaganeite formation [45].

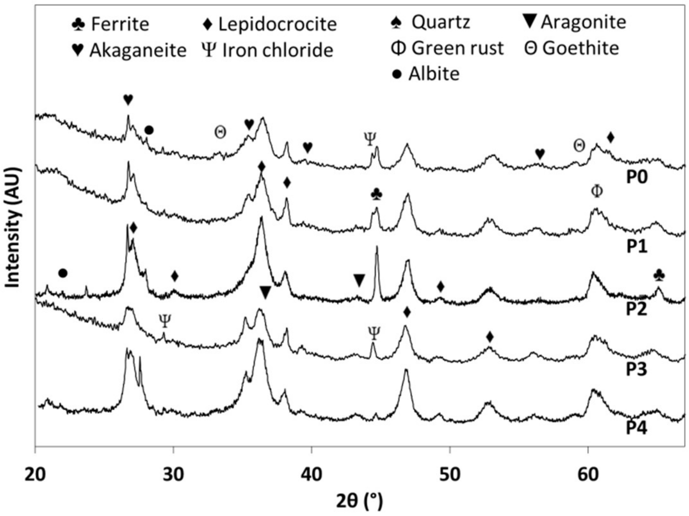

Figure 16. XRD patterns of carbon steel coupons after 241-day exposure in all sites.

3.6. Remarks on Corrosion Prevention and Pending Issues

Atmospheric corrosion in Northern Chile is a particular case of perpetual daily dry—wet cycling corrosion in the absence of rainfall. From the perspective of corrosion prevention in this region, metal coating is the only feasible technological alternative to be applied in carbon steel structures exposed to ambient conditions. However, important complementary issues must be considered at the moment of choosing the appropriate coating technique. Firstly, for structure installation, frequent fog-forming areas must be avoided to minimize the risk of corrosion by droplet precipitation. Secondly, adequate coating must be chosen to minimize the risk of dew-point condensation, and finally, coatings must cope with the high local solar irradiation.

The topography of the Atacama Desert is highly varied; it includes coastal and inland mountain ranges, isolated ridges and mesas, and broad interior valleys known for their salt flats, or dry salt lake beds. The present investigation was developed along flat areas where topographic effects are restricted to “shadowed areas” influenced by nearby hills or depressions. Thus, pending issues to be investigated are corrosion evolution within such relevant topographic accidents where geometric effects provoke interesting situations, such as long-standing fog that sustains isolated plant communities and the so-called adiabatic cooling effect that takes place alongside hill slopes.

4. Conclusions

Studying the atmospheric corrosion evolution of carbon steel AISI 1020 as coupons deposited in several sites along a transect in the Atacama Desert together with meteorological characterization, the following points can be emphasized:

- Vertical temperatures and *RH* gradients starting with low *RH* values at the ground level were observed in all sites;
- The vertical gradient generated a significant distortion in the *TOW* calculation when using *RH* values measured at the ground level. The use of *RH* values measured at 5 m above the ground level was found adequate for *TOW* determination;
- Water precipitation as small water droplets were demonstrated by using a fog water collector;
- The use of a limiting absolute humidity value is suggested instead of a limiting *RH* for the *TOW* determination;
- Metal corrosion in the Atacama Desert takes place as a sequence of wet—dry periods. The duration of wet periods is of a few hours during nighttime;

- Morphological examination showed that the corrosion was initiated by pits that gradually evolved to cover the complete metal surface in a maximum period of 250 days.
- It was found after 32 days of exposure a significant oxygen uptake in coupons oxide layer that was highest in the coastal site P0 and gradually decreased with the increasing distance from the coast. Similarly, but in lower extent, the chloride content in coupons decreased with the increasing distance from the coast. This is attributed to both relative humidity and saline marine fog intrusion from the coast.
- The oxide layer evolved in all sites to form a compact layer whose main constituents were lepidocrocite, goethite, and small amounts of akageneite. The corrosion depth can be modelled by a simple power function $d = At^B$ with $B < 1$, indicating a deceleration process.

Author Contributions: Conceptualization, L.C. and A.S.; methodology, L.C., A.S. and F.G.; validation, L.C. and A.S.; formal analysis, L.C.; investigation, L.C., A.S. and F.G.; writing—original draft preparation, L.C.; writing—review and editing, L.C., A.S. and F.G.; supervision, L.C. All authors have read and agreed to the published version of the manuscript.

Funding: This research was funded by CONICYT Chile (grant number: CeBiB FB-0001).

Institutional Review Board Statement: Not applicable.

Informed Consent Statement: Not applicable.

Data Availability Statement: The processed data are available from the corresponding author upon request.

Acknowledgments: The authors want to thank the strategic support received from the Chemical Engineering and Mineral Processing Department of the University of Antofagasta to carry on with field studies at the core of the Atacama Desert. Additionally, the authors wish to thank the Department of Metallurgy Engineering of the University of Atacama for the XRD and SEM analysis (projects: EQM 130125 and EQUV 003).

Conflicts of Interest: The authors declare no conflict of interest.

References

1. Schweitzer, A.P. Atmospheric Corrosion. In *Fundamentals of Metallic Corrosion. Atmospheric and Media Corrosion of Metals*, 2nd ed.; Schweitzer, P.A., Ed.; CRC Press Taylor & Francis Group: Boca Raton, FL, USA, 2007; pp. 39–66.
2. Oh, S.J.; Cook, D.C.; Townsend, H.E. Atmospheric corrosion of different steels in marine, rural and industrial environments. *Corr. Sci.* **1999**, *41*, 1687–1702. [CrossRef]
3. Di Sarno, L.; Majidian, A.; Karagiannakis, G. The effect of atmospheric corrosion on steel structures: A state-of-the-art and case-study. *Buildings* **2021**, *11*, 571. [CrossRef]
4. Cai, Y.; Xu, Y.; Zhao, Y.; Ma, X. Atmospheric corrosion prediction: A review. *Corros. Rev.* **2020**, *38*, 299–321. [CrossRef]
5. Morcillo, M.; Chico, B.; Díaz, I.; Cano, H.; de la Fuente, D. Atmospheric corrosion data of weathering steels. A review. *Corr. Sci.* **2013**, *77*, 6–24. [CrossRef]
6. Pei, Z.; Cheng, X.; Yang, X.; Li, Q.; Xia, C.; Zhang, D.; Li, X. Understanding environmental impacts on initial atmospheric corrosion based on corrosion monitoring sensors. *J. Mater. Sci. Technol.* **2021**, *64*, 214–221. [CrossRef]
7. Popova, K.; Prošek, T. Corrosion monitoring in atmospheric conditions: A review. *Metals* **2022**, *12*, 171. [CrossRef]
8. Rodríguez, J.J.S.; Hernández, F.J.S.; González, J.E.G. The effect of environmental and meteorological variables on atmospheric corrosion of carbon steel, copper, zinc and aluminium in a limited geographic zone with different types of environment. *Corros. Sci.* **2003**, *45*, 799–815. [CrossRef]
9. Almeida, E.; Morcillo, M.; Rosales, B. Atmospheric corrosion of zinc Part 1: Rural and urban atmospheres. *Br. Corros. J.* **2000**, *35*, 284–288. [CrossRef]
10. Morales, J.; Martín-Krijer, S.; Díaz, F.; Hernández-Borges, J.; González, S. Atmospheric corrosion in subtropical areas: Influences of time of wetness and deficiency of the ISO 9223 norm. *Corros. Sci.* **2005**, *47*, 2005–2019. [CrossRef]
11. Chico, B.; De la Fuente, D.; Díaz, I.; Simancas, J.; Morcillo, M. Annual atmospheric corrosion of carbon steel worldwide. An integration of ISOCORRAG, ICP/UNECE and MICAT databases. *Materials* **2017**, *10*, 601. [CrossRef]
12. de la Fuente, D.; Díaz, I.; Simancas, J.; Chico, B.; Morcillo, M. Long-term atmospheric corrosion of mild steel. *Corros. Sci.* **2011**, *53*, 604–617. [CrossRef]

13. Cereceda, P.; Osses, P.; Larrain, H.; Farías, M.; Lagos, M.; Pinto, R.; Schemenauer, R. Advective, orographic and radiation fog in the Tarapacá region, Chile. *Atmos. Res.* **2002**, *64*, 261–271. [CrossRef]
14. Klemm, O.; Schemenauer, R.S.; Lummerich, A.; Cereceda, P.; Marzol, V.; Corell, D.; van Heerden, J.; Reinhard, D.; Gherezghiher, T.; Olivier, J.; et al. Fog as a fresh-water resource: Overview and perspectives. *Ambio* **2012**, *41*, 221–234. [CrossRef]
15. Cereceda, P.; Larrain, H.; Osses, P.; Farías, M.; Egaña, I. The spatial and temporal variability of fog and its relation to fog oases in the Atacama Desert, Chile. *Atmos. Res.* **2008**, *87*, 312–323. [CrossRef]
16. McKay, C.P.; Friedmann, E.I.; Gómez-Silva, B.; Cáceres-Villanueva, L.; Andersen, D.T.; Landheim, R. Temperature and moisture conditions for life in the extreme arid region of the Atacama Desert: Four years of observations including the El Niño of 1997–1998. *Astrobiology* **2003**, *3*, 393–406. [CrossRef]
17. Beiderwieden, E.; Wrzesinsky, T.; Klemm, O. Chemical characterization of fog and rain water collected at the eastern Andes cordillera. *Hydrol. Earth Syst. Sci.* **2005**, *9*, 185–191. [CrossRef]
18. Straub, D.J.; Hutchings, J.W.; Herckes, P. Measurements of fog composition at a rural site. *Atmos. Environ.* **2012**, *47*, 195–205. [CrossRef]
19. Polkowska, Z.; Górecki, T.; Namieśnik, J. Determination of atmospheric pollutants in wet deposition. *Environ. Rev.* **2011**, *19*, 185–213. [CrossRef]
20. Navarro-González, R.; Rainey, F.A.; Molina, P.; Bagaley, D.R.; Hollen, B.J.; de la Rosa, J.; Small, A.M.; Quinn, R.C.; Grunthaner, F.J.; Cáceres, L.; et al. Mars-Like Soils in the Atacama Desert, Chile, and the Dry Limit of Microbial Life. *Science* **2003**, *302*, 1018–1021. [CrossRef]
21. Quinn, R.C.; Zent, A.P.; Grunthaner, F.J.; Ehrenfreund, P.; Taylor, C.L.; Garry, J.R.C. Detection and characterization of oxidizing acids in the Atacama Desert using the Mars Oxidation Instrument, Planet. *Space Sci.* **2005**, *53*, 1376–1388. [CrossRef]
22. Bull, A.T.; Asenjo, J.A. Microbiology of hyper-arid environments: Recent insights from the Atacama Desert, Chile. *Antonie van Leeuwenhoek* **2013**, *103*, 1173–1179. [CrossRef]
23. Cáceres, L.; Gómez-Silva, B.; Garró, X.; Rodríguez, V.; Monardes, V.; McKay, C.P. Relative humidity patterns and fog water precipitation in the Atacama Desert and biological implications. *J. Geophys. Res. Biogeosci.* **2007**, *112*, 1–11. [CrossRef]
24. *ASTM G1-90*; ASTM, 1999; p. 8. Available online: https://www.astm.org/DATABASE.CART/HISTORICAL/G1-03R11.htm (accessed on 5 August 2022).
25. Vargas, G.; Ortlieb, L.; Rutllant, J. Aluviones históricos en Antofagasta y su relación con eventos El Niño/Oscilación del Sur. *Rev. Geol. Chile* **2000**, *27*, 157–176.
26. Rutllant, J.A.; Fuenzalida, H.; Aceituno, P. Climate dynamics along the arid northern coast of Chile: The 1997–1998 dinámica del clima de la Región de Antofagasta (DICLIMA) experiment. *J. Geophys. Res. Atmos.* **2003**, *108*, 1–13. [CrossRef]
27. Wierzchos, J.; DiRuggiero, J.; Vítek, P.; Artieda, O.; Souza-Egipsy, V.; Škaloud, P.; Tisza, M.; Davila, A.F.; Vílchez, C.; Garbayo, I.; et al. Adaptation strategies of endolithic chlorophototrophs to survive the hyperarid and extreme solar radiation environment of the Atacama Desert. *Front. Microbiol.* **2015**, *6*, 934. [CrossRef]
28. Cordero, R.R.; Damiani, A.; Seckmeyer, G.; Jorquera, J.; Caballero, M.; Rowe, P.; Ferrer, J.; Mubarak, R.; Carrasco, J.; Rondanelli, R.; et al. The solar spectrum in the Atacama Desert. *Sci. Rep.* **2016**, *6*, 22457. [CrossRef] [PubMed]
29. Arenas-Díaz, F.; Fuentes, B.; Reyers, M.; Fiedler, S.; Böhm, C.; Campos, E.; Shao, Y.; Bol, R. Dust and aerosols in the Atacama Desert. *Earth-Sci. Rev.* **2022**, *226*, 103925. [CrossRef]
30. Pinto, R.; Barría, I.; Marquet, P.A. Geographical distribution of *Tillandsia* lomas in the Atacama Desert, northern Chile. *J. Arid Environ.* **2006**, *65*, 543–552. [CrossRef]
31. Qadir, M.; Jiménez, G.C.; Farnum, R.L.; Dodson, L.L.; Smakhtin, V. Fog Water Collection: Challenges beyond Technology. *Water* **2018**, *10*, 372. [CrossRef]
32. Schindelholz, E.; Kelly, R.G.; Cole, I.S.; Ganther, W.D.; Muster, T.H. Comparability and accuracy of time of wetness sensing methods relevant for atmospheric corrosion. *Corros. Sci.* **2013**, *67*, 233–241. [CrossRef]
33. Larson, J.W. General Corrosion. In *ASM Handbook. Corrosion Materials*, 1st ed.; Crammer, S.D., Covino, B.S., Eds.; ASM International: Novelty, OH, USA, 2005; p. 181.
34. Hoseinpoor, M.; Prošek, T.; Babusiaux, L.; Mallégol, J. Toward more realistic time of wetness measurement by means of surface relative humidity. *Corros. Sci.* **2020**, *177*, 33. [CrossRef]
35. *ISO 9223*; Corrosion of Metals and Alloys—Corrosivity of Atmospheres—Classification, Determination and Estimation. ISO: Geneva, Switzerland, 2012.
36. Cáceres, L.; De la Torre, J.; Gómez-Silva, B.; Rodríguez, V.; McKay, C.P. Atmospheric moisture collection from a continuous air flow through a refrigerated coil tube. *Atmos. Res.* **2004**, *71*, 127–137. [CrossRef]
37. Houston, J. Evaporation in the Atacama Desert: An empirical study of spatio-temporal variations and their causes. *J. Hydrol.* **2006**, *330*, 402–412. [CrossRef]
38. Treybal, R. *Operaciones de Transferencia de Masa*, 2nd ed.; McGraw-Hill: Ciudad de México, Mexico, 2000; pp. 254–264.
39. Morcillo, M.; Flores, S.; Salas, G.; Valencia, M. An extremely low corrosion rate of steel in the atmosphere of Cuzco (Peru). *Atmos. Environ. Part A Gen. Top.* **1993**, *27*, 1959–1962. [CrossRef]
40. Han, W.; Yu, G.; Wang, Z.; Wang, J. Characterization of initial atmospheric corrosion carbon steels by field exposure and laboratory simulation. *Corros. Sci.* **2007**, *49*, 2920–2935. [CrossRef]

41. Xiao, K.; Dong, C.; Li, X.; Wang, F. Corrosion products and formation mechanism during initial stage of atmospheric corrosion of carbon steel. *J. Iron Steel Res. Int.* **2008**, *15*, 42–48. [CrossRef]
42. Liu, J.; Fa, K.; Zhang, Y.; Wu, B.; Qin, S.; Jia, X. Abiotic CO_2 uptake from the atmosphere by semiarid desert soil and its partitioning into soil phases. *Geophys. Res. Lett.* **2015**, *42*, 5779–5785. [CrossRef]
43. Stratmann, M.; Bohnenkamp, K.; Engell, H.J. An electrochemical study of phase-transitions in rust layers. *Corros. Sci.* **1983**, *23*, 969–985. [CrossRef]
44. Tamura, H. The role of rusts in corrosion and corrosion protection of iron and steel. *Corros. Sci.* **2008**, *50*, 1872–1883. [CrossRef]
45. Xiao, H.; Ye, W.; Song, X.; Ma, Y.; Li, Y. Formation process of akaganeite in the simulated wet-dry cycles atmospheric environment. *J. Mater. Sci. Technol.* **2018**, *34*, 1387–1396. [CrossRef]